Mitigation of RF Impairments of a 160-GHz MMIC FMCW Radar Using Model-Based Estimation

Stephan Häfner, André Dürr, *Student Member, IEEE*, Christian Waldschmidt, *Senior Member, IEEE*, and Reiner Thomä, *Fellow, IEEE*

***Abstract*— Employing frequency bands above 100 GHz for future frequency-modulated continuous-wave (FMCW) radar applications necessitate hardware realizations as monolithic microwave integrated circuit (MMIC). Spurious signals stemming from hardware impairments deteriorate target detection performance, but hardware-based mitigation is not preferred, given the increased cost and size of the integrated circuits. Instead, signal processing-based mitigation is favored. In this article, an approach is proposed to mitigate hardware impairments by parametric, model-based signal processing. For one particular FMCW radar operating at 160 GHz, a behavioral model of the radar device is developed, which accounts for the hardware impairments. This device model is incorporated in the data model of a maximum-likelihood parameter estimator that both resolves target ranges and mitigates spurious signal components. The mitigation performance and the improved robustness of target detection of this approach in the presence of hardware impairments are demonstrated by measurements.**

***Index Terms*— Device model, dirty RF, frequency-modulated continuous-wave (FMCW) radar, Hammerstein model, model-based estimation, nonlinear model.**

I. Introduction

RADAR sensors are an emerging technology for autonomous driving or novel industrial, security, or medical applications. Given the need for increased bandwidth (e.g., several GHz) for imaging in crowded environments, higher frequency bands, such as the millimeter-wave spectrum, have to be considered.

Inevitable hardware impairments, such as nonlinearities, I/Q imbalances, or amplitude distortions, cause signal distortions, which result in, among others, deteriorated range estimates [1]–[3] or false detection [4], [5]. For example, the FMCW radar in [4] suffers from spurious signal components. The large amplitudes of these spurious signal components in the range profile make these indistinguishable from real targets, resulting in false detections. One possible mitigation of spurious signal components is by additional analog filtering of the transmit signal. However, given the high frequencies and the demand for low cost and compact realizations, the radar will be implemented in a MMIC [4], [6], rather than in discrete hardware. Hardware-based mitigation increases size and costs of the MMIC, which is not compatible with a compact and low-cost realization.

An alternative to analog domain mitigation is mitigation by signal processing in the digital domain. This saves on hardware costs at the expense of an increase in computational complexity. In communication engineering, signal processing-based mitigation of hardware impairments is known as dirty RF [7], [8], an expression which is adopted in this article for radar applications. There is a paradigmatic difference between communications and radar, though, which is relevant for the application of dirty RF. In communications, the information transported by the transmit signal is of interest. Hence, dirty RF in communications strives to equalize the received signal [9] in order to restore the actually transmitted information. In contrast, radar applications have a system identification aspect. The transmit signal is known and carries no information, but the propagation channel is of interest, i.e., parameters of the targets (e.g., target ranges) in the propagation channel. Therefore, equalizing the received signal is not a major concern. As a result, the dirty RF paradigm known from communication engineering has to be modified for accommodating the concerns of radar applications.

In this article, we will present an approach that combines dirty RF with the estimation of target parameters. The monostatic MMIC FMCW radar described in [10] will be taken as an example for implementing and demonstrating the new approach. We derive a behavioral model for the radar device, which properly describes the effects of the radar hardware on the received baseband signal. By incorporating this device model in a maximum-likelihood (ML) parameter estimator, mitigation of spurious signal components and estimation of target ranges are jointly achieved. The mitigation of spurious signals prevents false detection of targets, making the radar application more robust against hardware impairments. Measurements show the mitigation performance and enhanced target detection robustness.

This article is organized as follows: The problem under consideration is presented in Section II, illustrated by measurements in four scenarios. In Section III, distortion in the

Manuscript received July 18, 2019; revised September 23, 2019; accepted September 24, 2019. The work of S. Häfner and A. Dürr is supported by the German Research Foundation (DFG) under Grant TH 494/27-1 and Grant WA 3506/8-1. *(Corresponding author: Stephan Häfner.)*

S. Häfner and R. Thomä are with the Electronic Measurements and Signal Processing Group, Technical University Ilmenau, 98684 Ilmenau, Germany (e-mail: stephan.haefner@tu-ilmenau.de; reiner.thomae@tu-ilmenau.de).

A. Dürr and C. Waldschmidt are with the Institute of Microwave Engineering, Ulm University, 89081 Ulm, Germany (e-mail: andre.duerr@uni-ulm.de; christian.waldschmidt@uni-ulm.de).

Color versions of one or more of the figures in this article are available online at http://ieeexplore.ieee.org.

Digital Object Identifier 10.1109/TMTT.2019.2950204

TABLE I
RADAR SETTINGS FOR THE MEASUREMENTS

Centre frequency	157 GHz
Bandwidth	16 GHz
Sweep time	1 ms
ADC sampling rate	25 MHz

TABLE II
RANGES AND RCSS OF THE PLACED CORNER REFLECTORS FOR THE FOUR MEASUREMENT SCENARIOS

Scenario No.	Target range (m)	Target RCS (dBsm)
1	3	15.8
2	3.05	15.8
2	4.05	7
3	3	15.8
3	3.81	-10
4	2.87	7
4	3.6	-10
4	4.37	7

transmit signal, as caused by hardware impairments, is analyzed. A nonlinear, static device model will be subsequently derived, parameterized, and validated in Section IV. In order to account for frequency dependence and dynamic effects in the radar device, the device model will be extended to a dynamic nonlinear one. The model derivation and model parameterization are presented in Section V. In Section VI, measurements are used to compare the mitigation performance and the enhanced target detection robustness with predictions from the model. Section VII concludes this article.

The following mathematical notation is used to denote scalars, vectors, and matrices: Scalars are italic letters $(m, \ldots, M, \ldots, \tau)$, column vectors are written as boldface lower case $(\mathbf{a}, \ldots, \boldsymbol{\tau})$, and boldface capitals correspond to matrices $(\mathbf{A}, \ldots, \boldsymbol{\Sigma})$. The matrix operations $(\bullet)^T$ and $(\bullet)^\dagger$ denote the transpose and Moore–Penrose pseudoinverse, respectively. The imaginary unit is $\jmath = \sqrt{-1}$.

II. MEASUREMENTS AND PROBLEM STATEMENT

Calibration measurements, hence, measurements under well-known settings and conditions, were conducted in an anechoic chamber. As a radar system, the multiple-input multiple-output MIMO FMCW radar presented in [10] has been used, whereas only one channel has been captured and processed. The basic parameter settings of the radar are shown in Table I. Sequentially, three corner reflectors with varying radar cross section (RCS) and distance are placed as targets in front of the radar system. In total, four measurement scenarios were set up. Table II summarizes the ranges and RCS of the placed targets for the four measurement scenarios. Fig. 1 shows the radar system and two placed targets in the anechoic chamber.

Because the radar device is monostatic (transmitter and receiver antennas are closely located), strong leakage or crosstalk occurs. High-pass filtering is applied as preprocessing step to suppress the corresponding beat frequencies, and the analytic signal is calculated afterward. The range profile (magnitude squared of the range spectrum) of an example measurement with two targets is shown in Fig. 2. The highest beat frequency peaks can be assigned to the target ranges. Additional beat frequency peaks are visible, indicating the presence of further scatterers/reflectors. However, these beat frequencies cannot be assigned to the location of an object or multipath propagation. Hence, it is concluded that these beat frequencies are not due to scattering, such that they are ghost targets. Ghost targets will be defined as beat frequencies, which occur in conjunction with the beat frequency of a true target. Due to the presence of multiple beat frequencies for a single target, the number of targets may be overestimated by a detector.

The ghost targets are hardware caused and, therefore, deterministic and predictable. Hence, they can be accounted for in the target detection step by, e.g., excluding the respective peaks in the range profile. However, if a true target peak is hidden or intersected by a ghost target peak, the true target cannot be detected. Hence, this approach may fail in the case of multiple targets. In [5], the occurrence of ghost targets was tackled by limiting the bandwidth in a postprocessing step. However, bandwidth limitation causes a decrease in range resolution, such that this approach is also not appropriate. Hence, an approach is required which: 1) detects the true targets and 2) mitigates the ghost targets.

III. SIGNAL SYNTHESIZER ANALYSIS

A block chart of the transmit signal synthesizer, which generates the linear FMCW transmit signal (also called chirp or ramp), is shown in Fig. 3. A ramp oscillator (RO) signal, which is a linear frequency swept signal, is upconverted by mixing with a local oscillator (LO) signal [4]. The RO and LO signals are assumed as perfect, such that the respective signal models are

$$w_{\mathrm{RO}}(t) = U_{\mathrm{RO}} \cdot \cos\left(\pi \frac{B_{\mathrm{RO}}}{T_{\mathrm{RO}}} t^2 + 2\pi f_{\mathrm{RO}} t + \varphi_{\mathrm{RO}}\right) \quad (1a)$$

$$w_{\mathrm{LO}}(t) = U_{\mathrm{LO}} \cdot \cos\left(2\pi f_{\mathrm{LO}} t + \varphi_{\mathrm{LO}}\right). \quad (1b)$$

The parameters B_{RO} and T_{RO} are bandwidth and sweep time of the RO signal, respectively; and frequency f_{RO} is the center frequency. The LO frequency is denoted by variable f_{LO}. For the radar under consideration, the frequencies are: $B_{\mathrm{RO}} = 4$ GHz, $f_{\mathrm{RO}} = 10$ GHz, and $f_{\mathrm{LO}} = 58.5$ GHz. Phase terms φ_{LO} and φ_{RO}, and amplitudes U_{LO} and U_{RO} are the initial phase and amplitudes of the LO and RO signals, respectively. The phase terms are omitted in the following for sake of convenience.

Before the mixing step, the LO and RO signal are up converted by multipliers in order to increase the bandwidth (RO signal) and the center frequency (LO signal). Multipliers are nonlinear devices, and hence their input–output relation is a nonlinear transfer function. A common model for the input–output relation of nonlinear devices is the memory-less power series model [11], which is actually the Taylor series approximation of the nonlinear transfer function. Applying the power series model to the RO and LO signals yields

$$s_{\mathrm{RO}}(t) = \sum_{m=1}^{M} a_m \cdot U_{\mathrm{RO}}^m \cdot \cos\left(\pi m \frac{B_{\mathrm{RO}}}{T_{\mathrm{RO}}} t^2 + 2\pi m f_{\mathrm{RO}} t\right) \quad (2a)$$

$$s_{\mathrm{LO}}(t) = \sum_{n=1}^{N} b_n \cdot U_{\mathrm{LO}}^n \cdot \cos(2\pi n f_{\mathrm{LO}} t) \quad (2b)$$

(a) (b)

Fig. 1. (a) Radar system and (b) two corner reflectors acting as targets in the anechoic chamber.

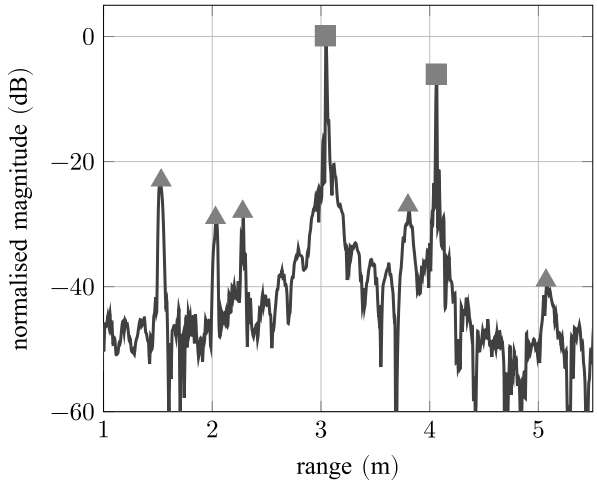

Fig. 2. Measured range profile according to measurement scenario 2 (see Table II). Beat frequency peaks are present for the distance of the true targets (square mark) and ghost targets (triangle mark).

with M and N the degrees of nonlinearity and a_m and b_n the power series coefficients. As a result, the output signals of the multipliers are multiple harmonics of the input signals, rather than just the upconverted signals for $n = 4$ and $m = 2$. In the following, the summation limits will be omitted for notational convenience.

Assuming an ideal mixer, the transmit signal becomes

$$s(t) = \sum_n \sum_m a_m \cdot U_{\mathrm{RO}}^m \cdot b_n \cdot U_{\mathrm{LO}}^n \cdot \cos\left(2\pi t n f_{\mathrm{LO}}\right) \cdot \cos\left(\pi m \frac{B_{\mathrm{RO}}}{T_{\mathrm{RO}}} t^2 + 2\pi m f_{\mathrm{RO}} t\right). \quad (3)$$

The assumption of an ideal mixer is not crucial, because a nonideal mixer causes additional harmonics, which can be accounted for by adjusting the degrees N and M of the nonlinearities. Applying trigonometric identity[1] yields

$$s(t) = \sum_n \sum_m c_{n,m} \cdot \left[\cos\left(\phi_{n,m}^+(t)\right) + \cos\left(\phi_{n,m}^-(t)\right)\right] \quad (4)$$

[1] $\cos x \cos y = 0.5 \cdot [\cos(x - y) + \cos(x + y)]$.

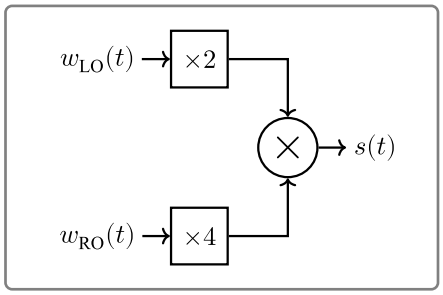

Fig. 3. Sketch of the signal generator, realized as an offset synthesizer [4].

with

$$c_{n,m} = \frac{a_m}{2} \cdot U_{\mathrm{RO}}^m \cdot b_n \cdot U_{\mathrm{LO}}^n \quad (5a)$$

$$\phi_{n,m}^+(t) = 2\pi t n f_{\mathrm{LO}} + \pi m \frac{B_{\mathrm{RO}}}{T_{\mathrm{RO}}} t^2 + 2\pi t m f_{\mathrm{RO}} \quad (5b)$$

$$\phi_{n,m}^-(t) = 2\pi t n f_{\mathrm{LO}} - \pi m \frac{B_{\mathrm{RO}}}{T_{\mathrm{RO}}} t^2 - 2\pi t m f_{\mathrm{RO}}. \quad (5c)$$

Summarized, the transmit signal $s(t)$ constitutes of multiple FMCW signals, which are at different frequency ranges and have different bandwidths. Fig. 4 shows the frequency-time diagram of the transmit signal for nonlinearity degrees $M = 6$ and $N = 3$. The highlighted area and the colored lines show the operating frequency range and the actually transmitted ramps for the radar under consideration, respectively.

IV. Nonlinear Static Device Model

A behavioral device model can be derived by calculating the baseband signal, while considering the transmit signal model and the propagation model $h(t)$. The considered propagation model is [5]

$$h(t) = \sum_p \gamma_p \cdot \delta(t - \tau_p) \quad (6)$$

with delay τ_p, which is proportional to the range r_p of the target [12], and weight γ_p, which accounts for attenuation. The resulting baseband signal for the pth target is

$$x(t) = \gamma_p \cdot \sum_{m_1} \sum_{m_2} \sum_{n_1} \sum_{n_2} \zeta \cdot \cos[2\pi f_{\mathrm{beat}}(t, \tau_p)t + \phi] \quad (7)$$

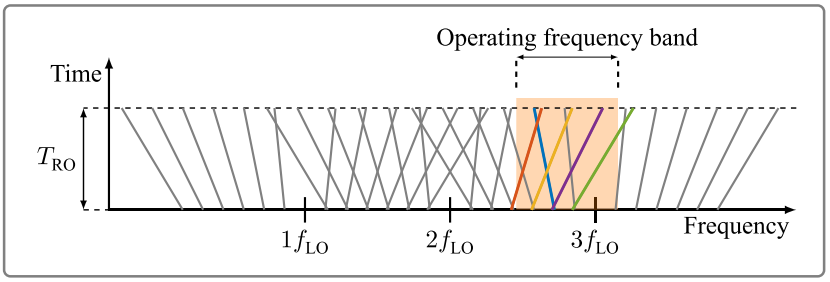

Fig. 4. Frequency-time diagram of generated FMCW signals for nonlinearity degrees of the RO and LO multipliers of $M = 6$ and $N = 3$, respectively. The colored ramps indicate the transmitted ramps, and the yellow ramp is the wanted ramp. The orange highlighted area denotes the operating frequency band of the radar.

with beat frequency $f_{\mathrm{beat}}(t, \tau_p)$, ζ the power series coefficients, which are related to the power series coefficients of the RO and LO multiplier; and term ϕ, which accounts for remaining phase variations. Note that ζ, ϕ, and $f_{\mathrm{beat}}(t, \tau_p)$ depend on the summation indices, which were dropped for notational convenience. The beat frequency is given by

$$f_{\mathrm{beat}}(t, \tau_p) = \pm(n_1 - n_2) f_{\mathrm{LO}} \pm m_2 \frac{B_{\mathrm{RO}}}{T_{\mathrm{RO}}} \tau_p \pm (m_1 - m_2) f_{\mathrm{RO}} \pm (m_1 - m_2) \frac{B_{\mathrm{RO}}}{T_{\mathrm{RO}}} t. \quad (8)$$

Auto Terms: For the auto terms ($m = m_1 = m_2$ and $n = n_1 = n_2$), the beat frequency in (8) reduces to

$$f_{\mathrm{beat}}(t, \tau_p) = \pm m \frac{B_{\mathrm{RO}}}{T_{\mathrm{RO}}} \tau_p. \quad (9)$$

Consequently, each delay τ_p causes multiple beat frequencies, which depend on the nonlinearity degree m of the RO signal multiplier.

Cross Terms: Considering the cross terms ($m_1 \neq m_2$ and $n_1 \neq n_2$), the beat frequency varies over time. Only a portion of the beat signal will remain in the baseband if the beat frequency exceeds the low-pass cutoff frequency. Hence, the cross terms result in short-time distortions, which are broadband in the frequency domain, and hence, have only a minor influence on the range spectrum. Therefore, cross terms will be neglected.

So far, the nonlinearity degrees M and N have not been clarified yet. Basically, they depend on the degree of nonlinearity of the multiplier, which is unknown. According to the transmit signal model in (4), the generated FMCW signals are at different frequency ranges, see also Fig. 4. These frequency ranges are differently attenuated due to the bandpass characteristic of the radar device. Hence, the radar transmits only a subset of the generated FMCW signals. This subset is identified from calibration measurements with a single target because each peak in the range spectrum can be clearly assigned to a generated FMCW signal. Accordingly, the nonlinearity degrees are determined as $N = 3$ and $M = 5$.

Summarized, the receive signal consists of multiple beat frequencies per delay, which are caused by the multiple transmitted FMCW signals. A model for the baseband signal in the presence of P targets and in the noise-less case is

$$x(t) = \sum_{p=1}^{P} \gamma_p \cdot \sum_{m=2}^{5} \zeta_m \cdot \cos\left(2\pi m \frac{B_{\mathrm{RO}}}{T_{\mathrm{RO}}} \tau_p t + \phi_m\right). \quad (10)$$

A. Estimation of Power Series Coefficients

A complex-valued baseband signal will be considered to estimate the power series coefficients. In the noise-less case and the presence of P targets, the baseband signal is

$$x(t) = \sum_{p=1}^{P} \gamma_p \cdot \sum_{m=2}^{5} \alpha_m \cdot \exp\left(\jmath 2\pi m \frac{B_{\mathrm{RO}}}{T_{\mathrm{RO}}} t \tau_p\right) \quad (11)$$

with $\alpha_m = \zeta_m \cdot \exp(\jmath \phi_m)$ the complex-valued power series coefficients. The complex weight γ_p accounts for the attenuation [12] and remaining phase variations [13] due to propagation. For a monostatic radar, the complex weight is given by

$$\gamma(f_c, B) = \sqrt{\frac{\rho}{(4\pi)^3 \; f_c^2 \; c_0^2 (2\tau)^4}} \exp(-\jmath 2\pi f_c \tau) \exp\left(\jmath \pi \frac{B}{T} \tau^2\right) \quad (12)$$

with center frequency f_c, ρ the RCS of the target, and c_0 the propagation velocity. Because the transmitted FMCW signals operate at different frequency ranges, the attenuation and phase variations differ. Hence, a different weight γ has to be considered for each beat frequency. Accordingly, the model for the complex baseband signal becomes

$$x(t) = \sum_{p=1}^{P} \sum_{m=2}^{5} \alpha_m \cdot \gamma_{m,p} \cdot \exp\left(\jmath 2\pi m \frac{B_{\mathrm{RO}}}{T_{\mathrm{RO}}} t \tau_p\right). \quad (13)$$

A model for the observation of K data samples, which are stacked in vector $\mathbf{y} \in \mathbb{C}^K$, and a single target is

$$\mathbf{y} = \mathbf{E}(\tau) \cdot \mathrm{diag}\{\boldsymbol{\gamma}\} \cdot \boldsymbol{\alpha} + \mathbf{n}. \quad (14)$$

The operator $\mathrm{diag}\{\boldsymbol{\gamma}\}$ forms a diagonal matrix from the entries of vector $\boldsymbol{\gamma}$, and the matrix and vectors in (14) are given by

$$\mathbf{E}(\tau) = \exp\left(\jmath 2\pi \frac{B_{\mathrm{RO}}}{T_{\mathrm{RO}}} \tau \cdot \mathbf{t} \cdot \mathbf{m}^T\right) \quad (15a)$$

$$\boldsymbol{\gamma} = \begin{bmatrix} \gamma(3f_{\mathrm{LO}} - 2f_{\mathrm{RO}}, 2B_{\mathrm{RO}}) \\ \gamma(2f_{\mathrm{LO}} + 3f_{\mathrm{RO}}, 3B_{\mathrm{RO}}) \\ \gamma(2f_{\mathrm{LO}} + 4f_{\mathrm{RO}}, 4B_{\mathrm{RO}}) \\ \gamma(2f_{\mathrm{LO}} + 5f_{\mathrm{RO}}, 5B_{\mathrm{RO}}) \end{bmatrix} \quad (15b)$$

$$\boldsymbol{\alpha} = [\alpha_2, \alpha_3, \alpha_4, \alpha_5]^T. \quad (15c)$$

Vector $\mathbf{n}$ accounts for the measurement noise, $\mathbf{m} = [2, \ldots, 5]^T$, and vector $\mathbf{t} = [t_0, \ldots, Kt_0]^T$ comprises the sampling time instances, with t_0 the sampling interval

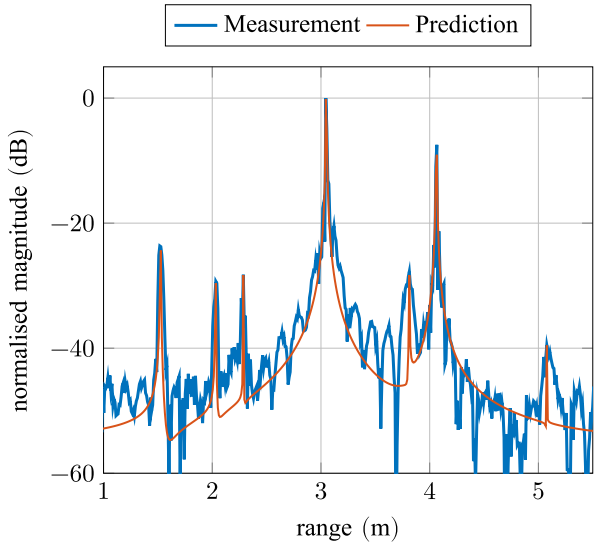

Fig. 5. Measured and predicted range profile for measurement scenario 2 (see Table II). The parameterized power series model and the known measurement settings (target ranges and RCSs) are used to predict the range profile.

of the ADC. Assuming proper complex, white and normally distributed noise, an estimate of the power series coefficients $\boldsymbol{\alpha}$ is given by the best-linear-unbiased estimator (BLUE) [14]

$$\hat{\boldsymbol{\alpha}} = [\mathbf{E}(\tau) \cdot \mathrm{diag}\{\boldsymbol{\gamma}\}]^{\dagger} \cdot \mathbf{y}. \tag{16}$$

A calibration measurement with a single target is used to estimate the power series coefficients $\boldsymbol{\alpha}$.

For verification of the power series model, the measured and predicted range spectrum for measurement scenario 2 of Table II is shown in Fig. 5. The prediction is conducted by using the estimated power series coefficients, and the known target positions and RCSs, and plugging in to (13). A good match of the peak height and peak position between measurement and prediction can be observed. However, the peak width does not match the measurements. The peak width indicates the presence of dynamic effects [11], which are due to the frequency dependence of, e.g., power amplifiers, transmission lines, splitters, and so on. Furthermore, the peak width varies for each beat frequency, because the corresponding ramps are at different frequency ranges, and therefore, undergo different parts of the frequency response of the radar device.

Summarized, the power series model properly describes the occurrence of multiple beat frequencies for a single scatterer. Because the power series model is a nonlinear static device model, amplitude, and phase distortion due to the frequency response of the radar device are not accounted for. Hence, a nonlinear and dynamic model becomes necessary in order to properly describe the radar device.

V. Nonlinear Dynamic Device Model

Joint consideration of dynamic effects and nonlinearities can be accomplished by the Volterra or Wiener theory [11]. Because the estimation of the Volterra or Wiener kernels is

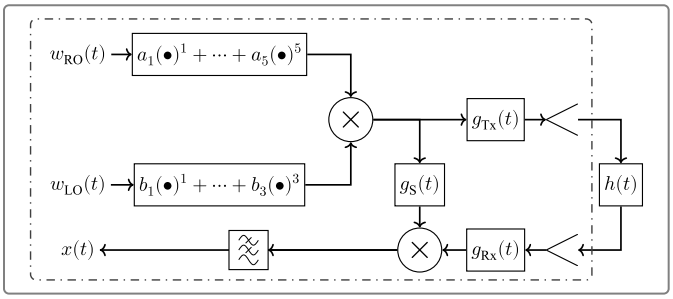

Fig. 6. Block chart of the device model with Hammerstein model at bandpass.

complicated, simplifications are commonly employed. Here, a Hammerstein model will be utilized, where the device is modeled as a serial cascade of two subsystems: a static nonlinear system followed by a dynamic linear system [11]. The static, nonlinear subsystem is described by a power series, as described in Section IV. The dynamic, linear subsystem is modeled by a linear time invariant (LTI) system. If different LTI systems are considered for different powers of the power series, the model is called generalized Hammerstein model. Subsequently, the Hammerstein model will be considered to describe the radar device at bandpass and baseband domains.

A. Hammerstein Model at Bandpass

A Hammerstein model at a bandpass domain is given by combining the power series model of the signal synthesizer, and the model presented in [5], which accounts for occurring device dynamics at bandpass level. The model structure is shown in Fig. 6. This model structure has a physical interpretation because the model components can be related to hardware components and their behavior in the real device. However, the measurements are at the baseband domain, such that the Hammerstein model at the bandpass domain is hard to identify. Therefore, a baseband model, which equivalently describes the device influence on the received signal, is necessary.

B. Generalized Hammerstein Model at Baseband

In order to transform the bandpass model in Fig. 6 into an equivalent baseband representation, several considerations have to be taken into account. First, the nonlinearities of the transmitter at bandpass can be equivalently represented by nonlinearities of the receiver at baseband, because only auto terms are considered at baseband and cross terms are neglected. Second, the generated FMCW signals are at different frequency ranges (see Fig. 4) and, therefore, are influenced by different parts of the radar transfer function at bandpass. Hence, each beat frequency at baseband is affected by a different device dynamic. Finally, these different device dynamics are assumed to be related to nonintersecting parts of the radar transfer function at bandpass. Summarized, an equivalent representation of the Hammerstein model at bandpass is given by a generalized Hammerstein model at baseband, whose

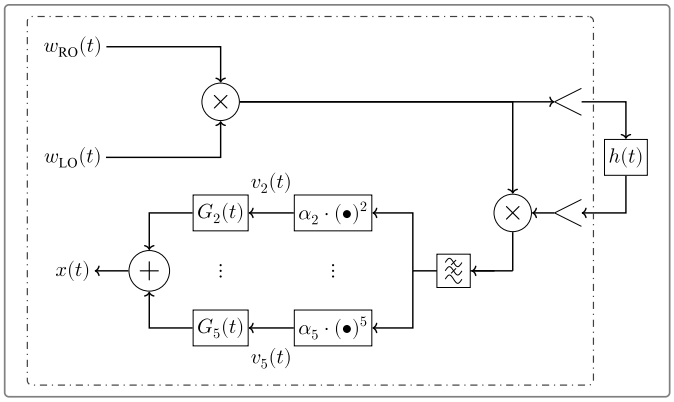

Fig. 7. Block chart of the device model with generalized Hammerstein model at baseband.

block chart is shown in Fig. 7. The corresponding baseband signal for P targets in the noise-less case is

$$x(t) = \sum_{p=1}^{P} \sum_{m=2}^{5} \alpha_m \cdot \gamma_{m,p} \cdot G_m(t) \cdot \exp\left(\jmath 2\pi m \frac{B_{\mathrm{RO}}}{T_{\mathrm{RO}}} t \tau_p\right) \quad (17)$$

with $G_m(t)$ the device dynamic at baseband. Note, that for an FMCW radar, a convolution with an LTI system at bandpass can be transformed to a multiplication with its frequency response at baseband [15]. Hence, $G_m(t)$ represents the device dynamic, which effects the transmitted FMCW signal causing the mth beat frequency.

Estimation of the model parameters α_m and $G_m(t)$ will be divided into the estimation of the power series coefficients α_m (identification of the static nonlinear subsystem) and determination of the device dynamics $G_m(t)$ (identification of the dynamic linear subsystem). The coefficients α_m are estimated by the BLUE, as stated in Section IV-A. Knowing the coefficients α_m, the input signal $v_m(t)$ to each system $G_m(t)$ is

$$v_m(t) = \alpha_m \cdot \gamma_m \cdot \exp\left(\jmath 2\pi m \frac{B_{\mathrm{RO}}}{T_{\mathrm{RO}}} t \tau\right). \quad (18)$$

Estimation of $G_m(t)$ from the output $x(t)$, while knowing the inputs $v_m(t)$, can be treated as the identification of a multiple-input single-output system with p-canonical structure [16]. Because four beat frequencies ($m = 2, \ldots, 5$) are present, four independent measurements would be necessary to estimate the device dynamic for all beat frequencies. However, if only one calibration measurement is taken into account, more unknowns than number of measurements would be present. Hence, a parametric model with a fewer number of parameters is required, in order to get a unique estimation result.

A parametric model for $G_m(t)$ is given by the rational form [17]

$$G_m(t) = \frac{x_m(t)}{v_m(t)} = \frac{b_{m,0} + \sum_{r=1}^{B_m} b_{m,r} \cdot p^r(t)}{1 + \sum_{r=1}^{C_m} c_{m,r} \cdot p^r(t)} \quad (19)$$

with coefficients $b_{m,r}, c_{m,r} \in \mathbb{C}$, and $p(t) = \jmath 2\pi t$. The best suited number $B_1, \ldots, B_M$ and $C_1, \ldots, C_M$ of numerator and denominator coefficients, and the coefficients $b_{m,r}$ and $c_{m,r}$ itself have to be determined from a calibration measurement. Estimation of the coefficients can be accomplished by minimizing the sum of squared errors between measurement and model [17]. However, minimizing the squared error with respect to (w.r.t) the number of coefficients is not considerable, because an increase of the model complexity always reduces the squared error [17]. Hence, a criterion is necessary, which validates the coefficient estimates in conjunction with the number of coefficients.

TABLE III
ESTIMATED NUMBER OF NUMERATOR B_m AND DENOMINATOR C_m COEFFICIENTS FOR THE MODEL OF $G_m(t)$ IN (19)

	$m=2$	$m=3$	$m=4$	$m=5$
B_m	11	11	20	09
C_m	07	08	11	08

The Bayesian information criterion (BIC) [16], which is a tradeoff between model accuracy (sum of squared errors) and model complexity (number of coefficients), will be used here. In order to jointly estimate the best-suited number of coefficients and the corresponding coefficients, the BIC has to be minimized. Because minimization of the BIC w.r.t all unknowns is a high-dimensional optimization problem, sequential optimization will be used to reduce computational complexity. For a known number of coefficients, the coefficients are estimated, and the BIC is calculated. Subsequently, the BIC is minimized subject to the number of coefficients. The genetic algorithm "ga" from MATLAB global optimization toolbox is used to minimize the BIC subject to the number of coefficients, whereas the system identification toolbox function "oe" is used to estimate the coefficients for a given number of coefficients. Because the number of coefficients is integers, integer optimization can be applied. A calibration measurement with a single target is used to estimate the number of coefficients and the corresponding coefficients itself.

The estimated number of the numerator and denominator coefficients are shown in Table III. In order to verify the device model, the measured and predicted range spectrum for measurement scenario 2 of Table II is shown in Fig. 8. The prediction is conducted by using the estimated model parameters, and the known target positions and RCSs, and plugging in to (17). A good match of the measured and predicted range profile is obvious. Hence, the generalized Hammerstein model properly describes the signal generation and transfer characteristics of the radar device.

VI. MEASUREMENT-BASED VERIFICATION

An ML parameter estimator [14] is chosen to estimate target ranges and path weights. Therefore, the vectors $\boldsymbol{\tau}$ and $\boldsymbol{\gamma}$ are introduced, which comprise the unknown delays τ_p and complex weights $\gamma_{m,p}$ of all targets, respectively. Assuming proper complex, normally distributed and white measurement

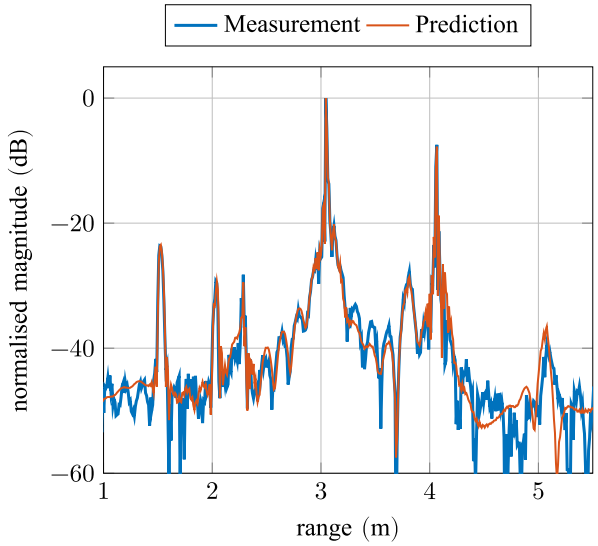

Fig. 8. Measured and predicted range profile for measurement scenario 2 (see Table II). The parameterized generalized Hammerstein model and the known measurement settings (target ranges and RCSs) are used to predict the range profile.

noise, the ML parameter estimator is given by the objective

$$\hat{\boldsymbol{\tau}}, \hat{\boldsymbol{\gamma}} = \min_{\boldsymbol{\tau},\boldsymbol{\gamma}} \sum_{k=1}^{K} \|y(k) - x(k; \boldsymbol{\tau}, \boldsymbol{\gamma})\|^2 \tag{20}$$

with $y(k)$ the sampled measurements and $x(k; \boldsymbol{\tau}, \boldsymbol{\gamma})$ the sampled model (17), depending on the unknown delays and weights. The number of data samples is $K = 610$. The optimization scheme presented in [18] is used to minimize the objective (20) and jointly determine the number P of targets. A proper determination of the number of targets (respectively, the order of the data model) is important for the parameter estimation quality [19]. An over fitting, hence, the estimation of more targets than are present severely deteriorates the estimation quality of the parameters of the true targets [20].

The measurement scenarios 1, 3, and 4 of Table II will be considered to validate the proposed approach. Table IV shows the deployed target ranges and the correspondingly occurring ghost target ranges, calculated from (9). Note that some target ranges were chosen such that ghost peaks and main peaks are close or intersecting in the range profile. For example, in scenario 4, the main peak of the first target (2.87 m) is close to a ghost peak at 2.73 m of the second target. A similar situation is present for scenario 3. These situations are worthwhile to consider in order to show the superiority of the proposed approach against, e.g., peak detection. The estimated target ranges, which are the wanted results of the radar application, are shown in Table IV as "estimated ranges." A good agreement between deployed and estimated ranges is obvious. Furthermore, the true number of targets is correctly determined in each case. Hence, the estimator can cope with the occurrence of ghost targets. In addition, the approach can detect targets even if they are hidden or intersected by ghost targets in the range profile.

TABLE IV

DEPLOYED TARGET RANGES, RANGES OF OCCURRING GHOST TARGETS, AND ESTIMATED TARGET RANGES FOR THREE MEASUREMENT SCENARIOS OF TABLE II

Scenario	Depl. range (m)	Ghost ranges (m)	Estim. range (m)
1	3	1.52, 2.28, 3.75	3.05
3	3	1.50, 2.25, 3.75	3.05
3	3.81	1.91, 2.86, 4.77	3.82
4	2.87	1.44, 2.15, 3.59	2.87
4	3.6	1.81, 2.73, 4.52	3.61
4	4.37	2.19, 3.28, 5.46	4.37

Fig. 9 shows the range profiles for measurement scenarios 3 and 4 of Table IV. In Fig. 9(a), the ghost peak at 1.5 m has a higher amplitude than the true target peak at 3.81 m. Hence, simple peak detection will detect the ghost peak first. However, the ghost peak at 1.5 m is related to the true target peak at 3 m, which is the highest peak in the range profile. The highest peak in the range profile always corresponds to a true target location. This is assured by the radar hardware, as the signal synthesizer is constructed to synthesize the corresponding ramp signal, and the hardware is optimized for the frequency band of this ramp. Accordingly, the parameter estimator works as follows: the highest peak is detected in the range profile (detection step), and the location of all corresponding ghost peaks is calculated using (9). Afterward, the target peak and the respective ghost peaks are removed from the measurements by plugging in the parameter estimates in the device model (17) and subtracting the parameterized device model from the measurements (mitigation step). As a result, these peaks will vanish or at least become highly attenuated in the range profile. Hence, the highest peak in the remaining range profile must correspond to the next true target. In Fig. 9, the predicted range profiles are calculated by plugging in all estimated delays $\hat{\boldsymbol{\tau}}$ and the estimated weights $\hat{\boldsymbol{\gamma}}$ in the data model (17), and applying Fourier transform afterward. A good agreement between predicted (red curve) and measured (blue curve) range profile is obvious. Hence, all ghost peaks were successfully predicted by the proposed dirty RF scheme. In the remaining range profile, which is the coherent difference of the measurements and the predictions, no significant peak remains. Hence, the ghosts are properly mitigated, and an overestimation of the number of targets is circumvented.

Summarized, the ML estimator, in conjunction with the proposed device model, properly detects all targets and mitigates the ghosts by exploiting the developed device model. Hence, this approach is more robust against the presence of ghost targets compared with, e.g., peak detectors. Because the ghost targets are mitigated, targets that are hidden by a ghost target in the range profile become detectable. This is a clear advantage compared with the methods which attempt to ignore ghost peaks in the range profile.

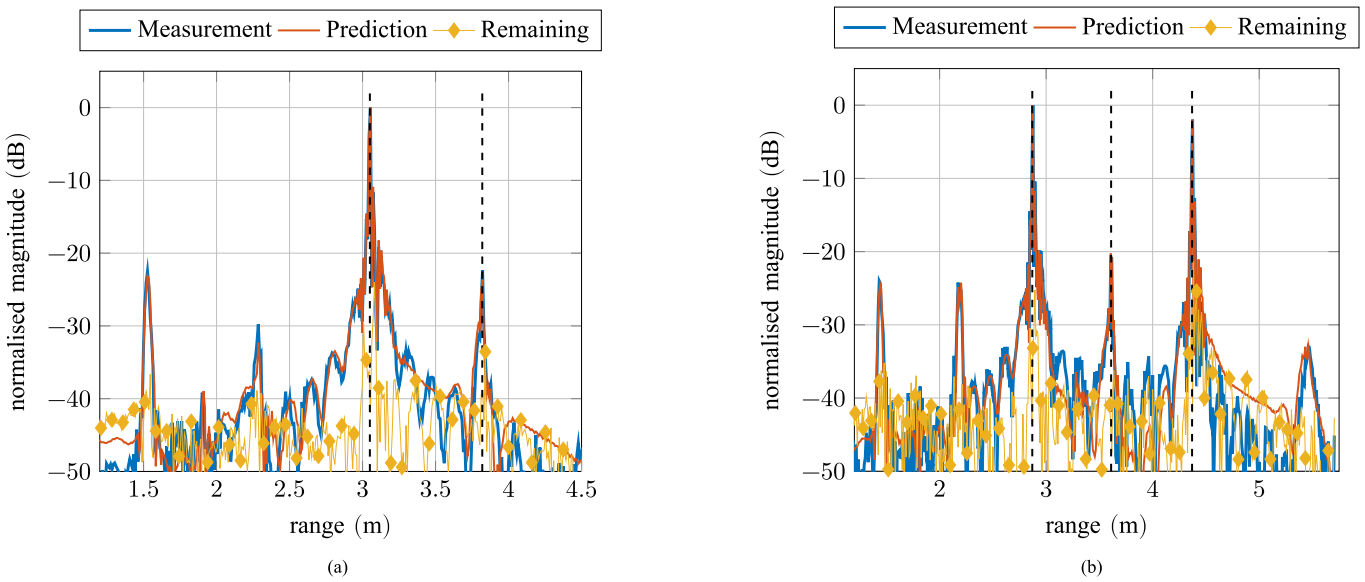

Fig. 9. Measured, predicted, and remaining range profiles for (a) measurement scenario 3 and (b) measurement scenario 4 of Table II. Ranges of the placed targets are indicated by black dashed lines. The estimated delays and weights from each measurement scenario are used to predict the respective range profiles.

VII. Conclusion

A new model-based signal processing approach to cope with spurious signal components in radar has been proposed, and exemplary implement for a 160-GHz MMIC FMCW radar. Spurious signals have been pointed out as a severe problem, as they deteriorate the target detection performance of the radar. The presented approach utilizes a ML parameter estimator, which exploits a data model of the measurements. The hardware caused spurious have been analyzed, and a device model has been developed to account for them in the data model. Measurements have been used to show the superiority of the new processing scheme. The parameter estimator is able to detect all targets and jointly mitigates the spurious signal components, making the radar more robust against hardware impairments. The proposed approach is not limited to the exemplary considered radar, as it can be applied to each radar by developing an appropriate device model.

Acknowledgment

The authors would like to thank Dr. W. Kotterman for his valuable comments and suggestions to improve this article.

References

[1] S. O. Piper, "Homodyne FMCW radar range resolution effects with sinusoidal nonlinearities in the frequency sweep," in *Proc. Int. Radar Conf.*, May 1995, pp. 563–567.

[2] M. Pichler, A. Stelzer, P. Gulden, and M. Vossiek, "Influence of systematic frequency-sweep non-linearity on object distance estimation in FMCW/FSCW radar systems," in *Proc. 33rd Eur. Microw. Conf.*, Oct. 2003, pp. 1203–1206.

[3] S. Ayhan, S. Scherr, A. Bhutani, B. Fischbach, M. Pauli, and T. Zwick, "Impact of frequency ramp nonlinearity, phase noise, and SNR on FMCW radar accuracy," *IEEE Trans. Microw. Theory Techn.*, vol. 64, no. 10, pp. 3290–3301, Oct. 2016.

[4] M. Hitzler *et al.*, "Ultracompact 160-GHz FMCW radar MMIC with fully integrated offset synthesizer," *IEEE Trans. Microw. Theory Techn.*, vol. 65, no. 5, pp. 1682–1691, May 2017.

[5] S. Häfner, A. Dürr, R. Thomä, C. Waldschmidt, and G. D. Galdo, "High-resolution parameter estimation for chirp-sequence radar considering hardware impairments," in *Proc. 11th German Microw. Conf. (GeMiC)*, Mar. 2018, pp. 355–358.

[6] M. Hitzler, P. Grüner, L. Boehm, W. Mayer, and C. Waldschmidt, "On monostatic and bistatic system concepts for mm-wave radar MMICs," *IEEE Trans. Microw. Theory Techn.*, vol. 66, no. 9, pp. 4204–4215, Sep. 2018.

[7] G. Fettweis, M. Löhning, D. Petrovic, M. Windisch, P. Zillmann, W. Rave, "Dirty RF: A new paradigm," *Int. J. Wireless Inf. Netw.*, vol. 14, no. 2, pp. 133–148, Jun. 2007.

[8] M. Grimm, "Dirty RF signal processing for mitigation of receiver front-end non-linearity," Ph.D. dissertation, Fac. Elect. Eng. Inf. Technol., TU-Ilmenau, Ilmenau, Germany, Oct. 2013.

[9] M. Grimm, M. Allen, J. Marttila, M. Valkama, and R. Thomä, "Joint mitigation of nonlinear RF and baseband distortions in wideband direct-conversion receivers," *IEEE Trans. Microw. Theory Techn.*, vol. 62, no. 1, pp. 166–182, Jan. 2014.

[10] A. Dürr *et al.*, "High-resolution 160-GHz imaging MIMO radar using MMICs with on-chip frequency synthesizers," *IEEE Trans. Microw. Theory Techn.*, vol. 67, no. 9, pp. 3897–3907, Sep. 2019.

[11] D. Schreurs, *RF Power Amplifier Behavioral Modeling* (The Cambridge RF and Microwave Engineering Series). Cambridge, U.K.: Cambridge Univ. Press, 2009.

[12] M. I. Skolnik, *Radar Handbook*, 2nd ed. New York, NY, USA: McGraw-Hill, 1990.

[13] M. A. Richards, *Fundamentals of Radar Signal Processing*, 2nd ed. Madison, WI, USA: McGraw-Hill, 2013.

[14] T. K. Moon and W. C. Stirling, *Mathematical Methods and Algorithms for Signal Processing*. London, U.K.: Prentice-Hall, 2000.

[15] S. Häfner and R. S. Thomä, "Identification of linear time invariant systems using FMCW signals and stretch processing receivers," *Int. J. Adv. Telecommun., Electrotechn., Signals Syst.*, vol. 8, no. 2, pp. 35–39, 2019.

[16] O. Nelles, *Nonlinear System Identification: From Classical Approaches to Neural Networks and Fuzzy Models*. Berlin, Germany: Springer, 2001.

[17] R. Pintelon and J. Schoukens, *System Identification: A Frequency Domain Approach*. Piscataway, NJ, USA: IEEE Press, 2001.

[18] S. Häfner *et al.*, "Contribution to drone detection by exploiting parameter estimation for a prototype mm-wave radar system," in *Proc. 22nd Int. ITG Workshop Smart Antennas (WSA)*, Mar. 2018, pp. 1–8.

[19] M. Landmann, M. Kaske, and R. S. Thoma, "Impact of incomplete and inaccurate data models on high resolution parameter estimation in multidimensional channel sounding," *IEEE Trans. Antennas Propag.*, vol. 60, no. 2, pp. 557–573, Feb. 2012.

[20] A. Richter, "Estimation of radio channel parameters: Models and algorithms," Ph.D. dissertation, Fac. Elect. Eng. Inf. Technol., TU-Ilmenau, Ilmenau, Germany, May 2005.

Stephan Häfner received the M.Sc. degree in computer engineering from Technical University Ilmenau, Ilmenau, Germany, in 2012, where he is currently pursuing the Ph.D. degree in the Electronic Measurements and Signal Processing Group.

His current research interest includes high-resolution parameter estimation for channel sounding and radar applications.

André Dürr (S'18) received the M.Sc. degree from Ulm University, Ulm, Germany, in 2017, where he is currently pursuing the Ph.D. degree.

From 2015 to 2016, he was an Intern with the Bosch Research and Technology Center North America, Palo Alto, CA, USA. In 2017, he joined the Institute of Microwave Engineering, Ulm University. His current research interests include novel imaging radar sensor concepts, phase noise mitigation, and performance degradation of noncoherent multichannel radar systems and their synchronization, all at millimeter-wave frequencies.

Mr. Dürr was a recipient of the Argus Science Award in 2015, the Verband der Elektrotechnik, Elektronik und Informationstechnik (VDE) Award in 2015, and the Verein Deutscher Ingenieure (VDI) Award in 2017.

Christian Waldschmidt (S'01–M'05–SM'13) received the Dipl.-Ing. (M.S.E.E.) and the Dr.-Ing. (Ph.D.E.E.) degrees from the Karlsruhe Institute of Technology, Karlsruhe, Germany, in 2001 and 2004, respectively.

From 2001 to 2004, he was a Research Assistant with the Institute of Radio Frequency Engineering and Electronics, Karlsruhe Institute of Technology. In 2004, he has been with Robert Bosch GmbH, Schwäbisch Gmünd, Germany, in the business units Corporate Research and Chassis Systems, where he was heading different research and development teams in microwave engineering, RF sensing, and automotive radar. In 2013, he returned to academia. He was appointed the Director of the Institute of Microwave Engineering, Ulm University, Ulm, Germany, and as a Full Professor. He has authored or coauthored over 100 scientific publications and over 20 patents. His current research interests include radar and RF sensing, millimeter-wave and submillimeter-wave engineering, antennas and antenna arrays, MIMO, RF, and array signal processing.

Prof. Waldschmidt served as the TPC Chair in 2015 and the TPC Co-Chair for the IEEE MTT-S International Microwave Symposium Conference for Intelligent Mobility in 2016. He is the Vice Chair of the IEEE MTT-27 Technical Committee (wireless-enabled automotive and vehicular applications), an Executive Committee Board Member of the German MTT/AP joint chapter, and a member of the Informationstechnische Gesellschaft (ITG) Committee Microwave Engineering. He was an Associate Guest Editor of the IEEE TRANSACTIONS ON MICROWAVE THEORY AND TECHNIQUES in 2015. He is currently a reviewer of multiple IEEE TRANSACTIONS and Letters.

Reiner Thomä (M'92–SM'99–F'07) received the Dipl.-Ing. (M.S.E.E.), Dr.-Ing. (Ph.D.E.E.), and the Dr.-Ing. (Habilitation) degrees in electrical engineering and information technology from Technische Universität Ilmenau, Germany, in 1975, 1983, and 1989, respectively.

From 1975 to 1988, he was a Research Associate in the fields of electronic circuits, measurement engineering, and digital signal processing with Technical University (TU) Ilmenau. From 1988 to 1990, he was a Research Engineer with the Center for Scientific Instrumentation, German Academy of Sciences at Berlin, Berlin, Germany. During this period, he was involved in the field of radio surveillance. In 1991, he spent a sabbatical leave at the Department of Telecommunications, University of Erlangen-Nuremberg. Since 1992, he has been a Professor of electrical engineering (electronics measurement) with TU Ilmenau, where he was the Director of the Institute of Communications and Measurement Engineering from 1999 to 2005. With his group, he has contributed to several European and German research projects and clusters, such as RESCUE, WINNER, PULSERS, EUWB, NEWCOM, COST 273, COST 2100, IC 1004, IRACON, EASY-A, and EASY-C. He became an Advisory Board Member of the EU mmMAGIC project. His current research interests include measurement and digital signal processing methods, including correlation and spectral analysis, system identification, sensor arrays, compressive sensing, time-frequency, and cyclostationary signal analysis, their application in mobile radio and radar systems, such as multidimensional channel sounding, propagation measurement and parameter estimation, MIMO-, millimeter-wave-, and ultrawideband (UWB) radars, measurement-based performance evaluation of MIMO transmission systems, including over-the-air testing in virtual electromagnetic environments, passive coherent location, and UWB radar sensor systems for object detection, tracking, and imaging.

Prof. Thomä is a member of the International Union of Radio Science (URSI) (Commission A) and VDE/ITG. Since 1999, he has been serving as the Chair for the IEEE-IM TC-13 on measurement in wireless and telecommunications. He is an IEEE Fellow and was a recipient of the Thuringian State Research Award for Applied Research, both for contributions to high-resolution multidimensional channel sounding. In 2014, he was a recipient of the Vodafone Innovation Award. He was the Speaker of the German nationwide DFG-focus project UKoLOS, Ultra-Wideband Radio Technologies for Communications, Localization, and Sensor Applications (SPP 1202).